J Appl Electrochem (2012) 42:857–866
DOI 10.1007/s10800-012-0452-y

ORIGINAL PAPER

The oxygen reduction reaction on Pt/TiO_xN_y-based electrocatalyst for PEM fuel cell applications

Wanli Wang · Oumarou Savadogo · Zi-Feng Ma

Received: 28 February 2012 / Accepted: 5 July 2012 / Published online: 8 August 2012

Abstract Titanium oxy-nitride was developed for the first time as Pt electrocatalyst support for the ORR in PEM fuel applications. The conditions of the support preparation and the Pt/TiO_xN_y-based electrodes' elaboration by chemical reduction method were determined. Comparison of the polarization curves of the carbon and the TiO_xN_y supported how clearly TiO_xN_y was more stable than the Vulcan XC-72R. It was found that the 40 wt% Pt/TiO_xN_y-based electrocatalyst is active for the ORR in acid medium, but the activity was less than that of Pt/C. The normalized electrochemical surface area degradation of Pt/TiO_xN_y was significantly less than that of Pt/C. The kinetics of the ORR on Pt/TiO_xN_y proceeded through a four-electron transfer process. The single-cell hydrogen/oxygen PEM fuel cell performances based on Pt/TiO_xN_y cathode electrocatalyst exhibited the same range of characteristics as those based on Pt/C.

Keywords New Pt electrocatalyst support · Titanium oxy-nitride · Electrocatalyst and support interaction · Oxygen reduction reaction (ORR) · PEM fuel cell · High stability

W. Wang · Z.-F. Ma
Department of Chemical Engineering, Institute of Electrochemical and Energy Technology, Shanghai Jiao Tong University, Shanghai 200240, People's Republic of China

W. Wang · O. Savadogo (✉)
Laboratory of New Materials for Electrochemistry and Energy, Department of Chemical Engineering, Ecole Polytechnique de Montréal, C. P. 6079, Succ. Centre-Ville, Montreal, QC H3C 3A7, Canada
e-mail: osavadogo@polymtl.ca

1 Introduction

In recent years, low-temperature proton exchange membrane (PEM) fuel cells, such as hydrogen/oxygen proton exchange membrane fuel cells (PEMFCs) and direct methanol/oxygen fuel cells (DMFCs), have been developed as promising energy technologies because of their inherent advantages of low operating temperature and fast start-up [1, 2]. However, several challenges still limit their commercialization. In PEMFC systems, the most common electrocatalysts used in both cathode and anode sides are platinum (or platinum alloys) supported onto carbon with a high surface [3]. But, it is now well established that the degradation of the carbon support at the platinum cathode electrocatalysts involved a number of drawbacks in the performance of the Pt/C system in PEM fuel cell applications. These drawbacks include platinum particle sintering, platinum dissolution, and carbon support corrosion, which are among the major failure modes for PEM fuel cell systems [4, 5].

The corrosion of the carbon supporting the cathode electrocatalyst in PMFC is responsible for removal of the carbon from the cell, which is responsible for the reduction of its content in the catalyst layer over time. This accelerates the platinum particle sintering because: (1) the cathode is held at relatively oxidative potentials, and oxygen atoms are being generated by the electrocatalyst particles; (2) the cells are at elevated temperature, and carbon atoms are able to react with oxygen atoms and/or water to generate gaseous products such as CO and CO_2, which leave the cell [6–8]. To overcome this degradation problem in the carbon support, several types of electrocatalyst support materials have been developed. These include: (1) multi-walled carbon nanotubes or grapheme [9], (2) novel substrates using inorganic metal oxides or

carbides with or without carbon, (3) metal oxide-based materials such as MnO_x [10], FeO_x [11], TiO_x [12–14], SiO_2 [15–18], WO_x [19, 20], NbO_2 [12, 21], ZrO_2 [22, 23], and indium tin oxide [24, 25], and (4) carbide materials such as tungsten carbide [26–29]. Some of them showed promising results as platinum electrocatalyst supports because they exhibit better specific activity than carbon supported platinum catalyst [30]. Unfortunately, their mass activity is usually lower because of the low surface area of metal oxides or carbides [30].

Titanium oxy-nitride has been developed as an attractive material for many electrochemical applications because of its specific properties, which can change with its N/O ratio. It was first reported by Sato as nitrogen-doped titania [31]. Since then, titanium oxy-nitride has been synthesized by various methods and employed in a wide range of applications. It can by synthesized by sputtering [32, 33], the ball milling method [34–36], CVD [37], TiN oxidation [38], sol–gel method [39–43], solvothermal synthesis [44], hydrothermal synthesis [45], and treating TiO_2 precursor directly under ammonia atmosphere [46–48]. Oxygen-rich titanium oxy-nitride with photoelectrochemical property has been widely used in photoelectrochemical devices [41] especially in solar selective absorbers that are able to improve the performance of the capture of visible light [45, 49] in solar energy transformation to heat. Nitrogen-rich titanium oxy-nitride qualified with high conductivity and stability has been used in diffusion barriers [50] and bipolar plates [32].

Accordingly, finding appropriate Pt support is one of the most important challenges facing the development of PEM fuel cells. In order to advance in seeking new approaches to solve this issue, titanium oxy-nitride is prepared in this study and used for the first time as the Pt electrocatalyst's support for PEM fuel cell applications.

In this study, platinum was deposited on titanium oxy-nitride by the chemical reduction method. Various electrochemical properties [(ORR) activity, kinetics, and durability] were determined. The possibility of titanium oxy-nitride acting as the catalyst's support in PEM fuel cells was suggested and will be proved in this work.

2 Experimental

All chemicals were purchased from Sigma-Aldrich. Prior to Pt/TiO_xN_y preparation, titanium oxy-nitride (TiO_xN_y) was synthesized by an anhydrous sol–gel method according to our previous study [51]. In brief, titanium (IV) isopropoxide and urea were mixed in isopropanol with the ratio of 1–4 at 80 °C for 12 h. Then, it was dried from 120 to 140 °C to form the precursor. The precursor was calcined under H_2/N_2 (2 % hydrogen/nitrogen, Liquid Air Canada) atmosphere at 800 °C for 2 h to obtain the TiO_xN_y powder. The fabrication was processed under nitrogen atmosphere to avoid the formation of oxides.

The Pt/TiO_xN_y was fabricated by the traditional chemical reduction process; 60 mg TiO_xN_y and $H_2PtCl_6{\cdot}6H_2O$ containing 40 mg platinum were dispersed into 50 mL water by ultrasonication to form the dispersion. The dispersion was then reduced by 0.1 M sodium borohydride added dropwise at room temperature for 2 h. Pt/TiO_xN_y powder was gathered by filtration through a mixed cellulose ester membrane filter (0.45 μm pore size), and then it was dried in air. For comparison, 40 wt% Pt/C was fabricated by the same procedure using Vulcan XC-72R (Cabot Corporation, USA) instead of TiO_xN_y.

The powder X-ray diffraction (XRD) measurement of the samples was recorded on an X-ray powder diffractometer (D/max-2200/PC, Rigaku Corporation, Japan) using CuKα radiation ($\lambda = 1.5406$ Å) with scattering angles (2θ) of 5°–80°. ASAP 2020 (Micromeritics Inc., USA) was used to determine the specific surface area of the samples. The morphologic property was characterized by TEM (JEM-2010HT, JEOL, Japan).

The electrochemical measurements were conducted in a three-electrode cell recorded using potentiostat/galvanostat model 273A (EG&G Princeton Applied Research, USA). Platinum mesh and saturated calomel electrode were used as the counter and reference electrodes, respectively. A solution of 0.5 M H_2SO_4 was employed as the electrolyte. The sample inks were prepared by mixing 10 mg sample powder with 0.45 mL deionized water, 0.03 mL isopropanol and 0.02 mL Nafion® solution (5 wt%, Dupont Company, USA), followed by sonication in a water bath for 10 min; 20 μL ink was dispensed and dried in air on the glassy carbon electrode ($\varphi = 0.5$ cm). The electrode was immersed in deaerated electrolyte and pretreated in cycles between −0.24 and 1 V at a scan rate of 100 mV s^{-1} for 100 cycles. The anodic polarization was studied by anodic linear sweep voltammetry from −0.05 (vs. open circuit voltage) to 1.76 V at a scan rate of 5 mV s^{-1}. This was used to evaluate the corrosion or degradation behavior of the support. The cyclic voltammetry performance of the supported platinum catalyst was determined under the same conditions as standard previous works [52, 53] in the range of potential between −0.24 and 0.96 V at a scan rate of 5 mV s^{-1}. Electrochemical surface area (ECSA) was calculated from the hydrogen adsorption–desorption peak of the CV profiles [54]. The accelerated durability was measured by cyclic voltammetry in the range of −0.24 to 0.96 V for 1,000 cycles at a scan rate of 50 mV s^{-1}. ORR performance was evaluated by the rotating disk electrode (RDE) technique. The polarization curves for the ORR were measured in an oxygen-saturated electrolyte by scanning the potential from 0.9 to 0.1 V at a scan rate of

5 mV s^{-1}. All potentials were reported with respect to the normal hydrogen electrode scale (NHE).

The gas diffusion layer for the cathode and the gas diffusion electrode (1.0 mg Pt cm^{-2}) for the anode were purchased from ElectroChem, Inc. The over-potential due to the anode half reaction can be neglected allowing the focus of PEM Fuel Cell improvement to be solely on the cathode side [55]. In the experiment of the present work, catalyst suspension was mixed with the supported platinum catalyst, Nafion (5 wt%, Dupont Company, USA), and isopropanol. The ratio in weight of the catalyst to the Nafion solution was 3:4. After being thoroughly dispersed, the suspension was brushed on the gas diffusion layer with a platinum loading of 0.4 mg cm^{-2} on the cathode electrode. Nafion 117 membrane (Dupont Company, USA) was pretreated by boiling in 5 % hydrogen peroxide for 1 h, then treated in 1 M sulfuric acid. After each step, the Nafion membrane was boiled in deionized water for 30 min. The prepared anode and cathode were positioned on both sides of the membrane and hot pressed at 2 tons and 110 °C for 4 min to form the membrane electrode assembly (MEA).

The PEM fuel cell was tested in a fuel cell testing unit with an active electrode area of 2.25 cm^2 (1.5 × 1.5 cm). The cell was operated at atmospheric pressure. The oxygen and hydrogen flow rate was 200 mL min^{-1}. The temperature of the cell was 50 °C. The current–voltage curves were collected after the activation process at a constant operation voltage of 0.6 V.

3 Results and discussion

Figure 1 shows the XRD spectra of the TiO_xN_y samples. The broad peaks of titanium oxy-nitride alone of the 2θ at

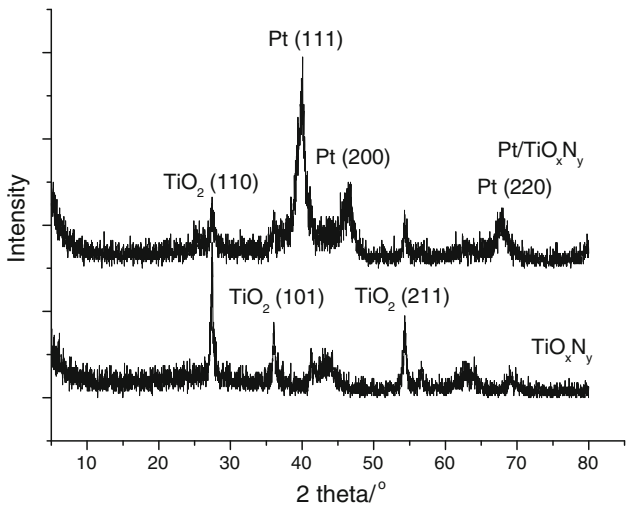

Fig. 1 XRD spectra of the TiO_xN_y and Pt/TiO_xN_y samples

27.44°, 36.08°, and 54.33° are assigned to (110), (101), and (211) facets, respectively, of the rutile structure of titanium dioxide (JCPDS No. 73-2224). The lattice constants are calculated as 4.5969 × 2.9541 Å, which is caused by the doping of nitrogen atoms [39, 56]. All the peaks of titanium oxy-nitride are also seen in the XRD spectrum of the Pt/TiO_xN_y sample. On the other hand, peaks of platinum are also observed on the XRD spectrum of the Pt/TiO_xN_y, which indicates that the platinum particles are deposited on titanium oxy-nitride. The peaks at the 2θ of 39.9°, 46.4°, and 67.7° are in agreement with the standard card of cubic structure of platinum (JCPDS No. 87-0640) assigned to (111), (200), and (220) facets, respectively. The crystallite size is calculated from the following Scherer equation:

$$D = \frac{K\lambda}{\beta \cos\theta} \quad (1)$$

D is the crystallite size, K is the Scherer constant which equals 0.89, β is the peak width at half height, θ is the angle of diffraction, and λ is the wavelength of incident X-ray which is 0.154056. The crystallite size of platinum is calculated as 8.4 nm. Titanium oxy-nitride has a tetragonal structure and platinum a cubic structure. The calculated lattice constants of titanium oxy-nitride without platinum are $a = b = 4.5663$ Å and $c = 2.9076$ Å, whereas those of titanium oxy-nitride with platinum are $a = b = 4.5851$ Å and $c = 2.9563$ Å for TiO_xN_y and $a = b = c = 3.9134$ Å for Pt. These values show clearly that the titanium oxy-nitride's lattice constants change when Pt electrocatalyst is deposited on it. These changes in the TiO_xN_y lattice constant in the presence of Pt suggest an interaction between the titanium oxy-nitride support and the platinum particles. On the other hand, the lattice constant of platinum is slightly larger than the standard which is 3.911 Å. This also supports the interaction between the Pt particles with the titanium oxy-nitride support.

Figure 2 shows the anodic polarization curves in 0.5 M sulfuric acid of titanium oxy-nitride and Vulcan XC-72R. For carbon, the high current observed is not related to the oxygen evolution reaction (OER) because carbon is not active for the OER. It is related to the corrosion behavior of carbon in acid medium [4]. The mass loss determined by weighing the mass of the electrode before and after polarizing it at 1.7 V for 10 days is 2 % of the initial mass.

In the case of the anodic polarization curve of the titanium oxy-nitride, there is an OER reaction in a high potential (we saw the gas bubbling from the electrode during the polarization). This behavior may also indicate the high stability of this electrode in this range of potential. This was supported by the evaluation of the stability of the electrode through the measurement of the mass loss (weighting the mass of the electrode before and after

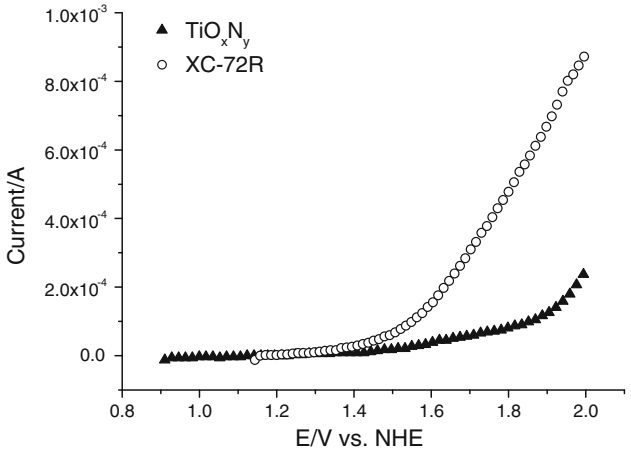

Fig. 2 Anodic polarization curves in 0.5 M sulfuric acid of titanium oxy-nitride and Vulcan XC-72R

polarizing it at 1.7 V for 10 days) which indicates no mass loss. Accordingly, the values of the current exhibited on these curves in Fig. 2 can be used to evaluate the relative corrosion behavior of TiO_xN_y material in sulfuric acid medium in comparison to carbon electrode.

The anodic or corrosion currents of both materials are small at low anodic potentials. At the potential above 1.4 V, however, this current for Vulcan XC-72R increased rapidly. In contrast, a smaller increase in the corrosion current is observed for titanium oxy-nitride at a potential of 1.6 V. This indicates that titanium oxy-nitride is more corrosion resistant than carbon black. It is known that the instantaneous voltage of a PEM fuel cell can reach more than 1.5 V during real operating conditions. At such a high potential, the stability of carbon is relatively poor and will cause problems of support corrosion and hence, platinum dissolution. But, it can be anticipated that the problems will be relieved using titanium oxy-nitride instead of carbon because the corrosion resistance of titanium oxy-nitride is much higher than that of carbon.

The corrosion of carbon occurs according to the following equations [57]:

$$C + 2H_2O \rightarrow CO_2(g) + 4H^+ + 4e^- \quad E^0 = 0.21\,V$$

$$C + 2H_2O \rightarrow CO(g) + 2H^+ + 2e^- \quad E^0 = 0.52\,V$$

Furthermore, during the cycling, the dominant surface group is reported as C–O functional group [57]. Hence, there is also generation of gaseous oxides such as CO or CO_2 gases. The oxidation peak observed in Fig. 3 after cycling (100 cycling) of carbon alone supports carbon degradation well. On the other hand, titanium oxy-nitride maintains the capacity of 190 F g^{-1}, and no oxidation or reduction peak is observed during the cycling. It can be concluded that titanium oxy-nitride is stable in the PEM fuel cell operating conditions.

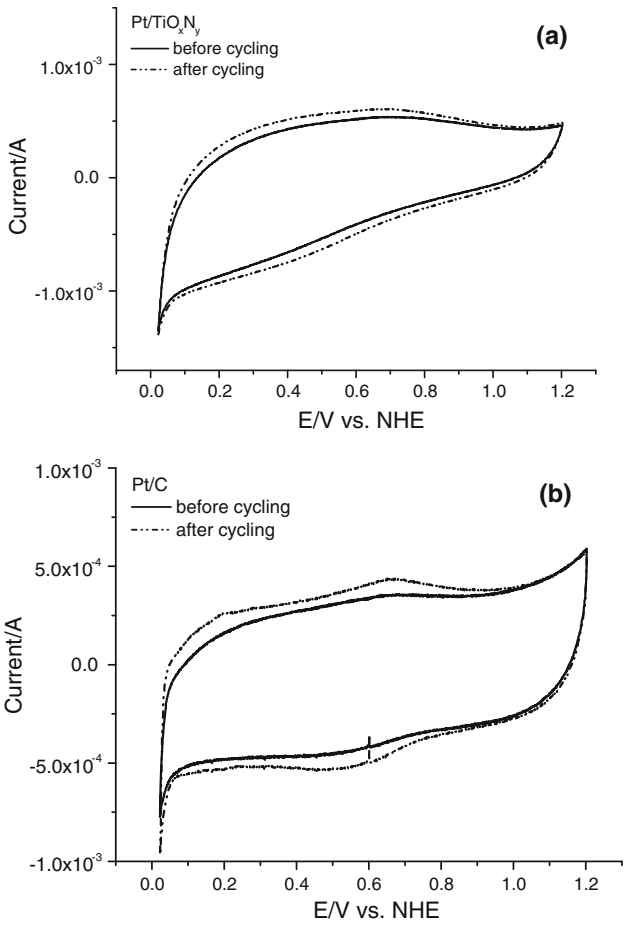

Fig. 3 Cyclic voltammetry curves of **a** titanium oxy-nitride and **b** Vulcan XC-72R before and after cycling 100 times

Figure 4 shows the TEM images of Pt/TiO_xN_y and Pt/C. The images show that titanium oxy-nitride exhibits a tetragonal structure. The particle size of titanium oxy-nitride is about 50–100 nm as shown in Fig. 4a. After depositing, platinum particles insert into the titanium oxy-nitride particles. The particle size of platinum observed from TEM is about 6–10 nm (Fig. 4b), which agrees well with the results from the XRD. The lattice distance can be observed clearly as 2.27 Å (shown in Fig. 4c) which is almost the same as the standard ($d = 2.26$ Å). The platinum particles are dispersed well on the support; furthermore, some of the particles are embedded in the support. This structure is different from that of Pt/C where platinum particles are adhered on the surface of carbon sphere in Pt/C catalyst. In Pt/C catalyst, carbon sphere offers a larger surface area as well as good probability of collision between oxygen atoms and platinum particles. However, this structure also contributes to the agglomeration of platinum particles because the surface energy is subject to minimization. On the other hand, titanium oxy-nitride might be similar to a layer structure which helps to avoid

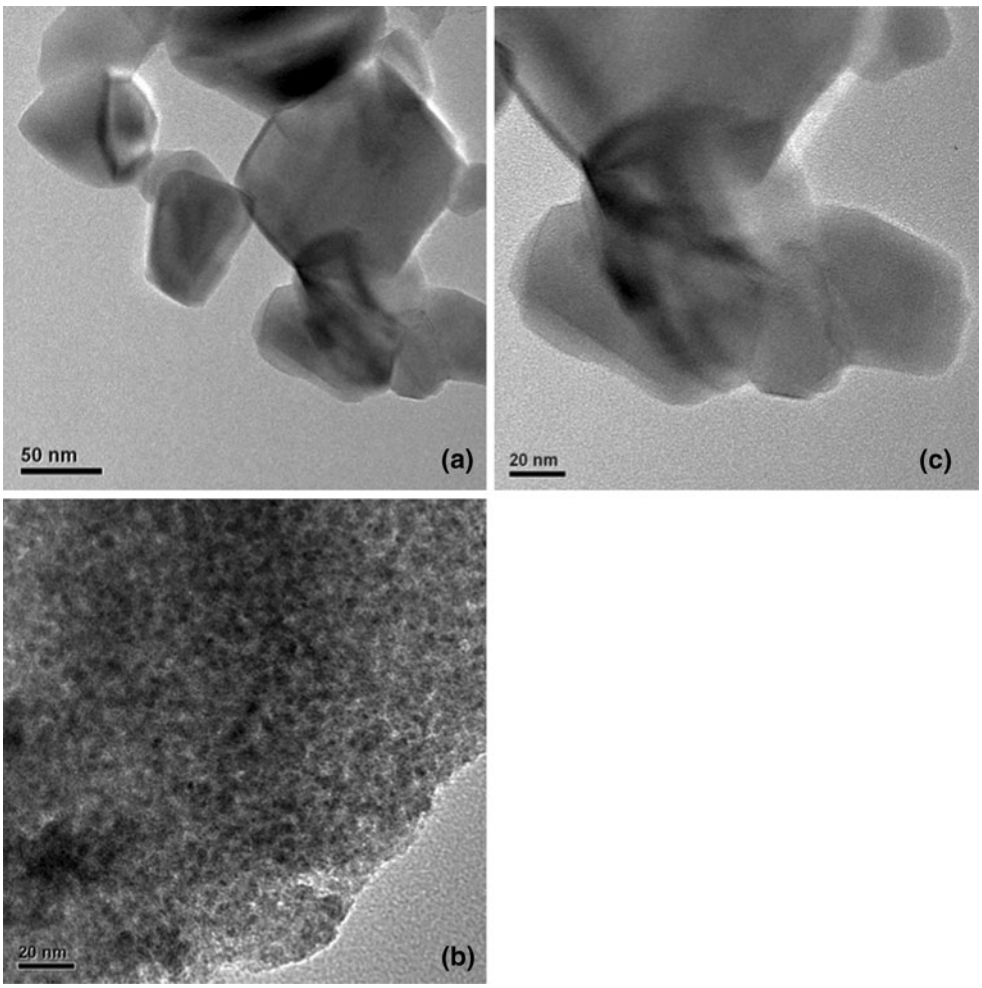

Fig. 4 TEM images of **a** titanium oxy-nitride, and **b**, **c** Pt/TiO_xN_y

this tendency. In this case, platinum particles which are deposited on titanium oxy-nitride have less opportunity for colliding with each other since the forces between platinum and support forbid aggregation. Nevertheless, this structure also reduces the probability of collision between oxygen atoms and platinum particles which might prevent the oxygen diffusion process.

In order to investigate the possibility of using titanium oxy-nitride as the catalyst's support in PEM fuel cells, cyclic voltammetry of platinum electrocatalyst supported on carbon and titanium oxy-nitride is shown in Fig. 5. This figure helps to understand the role of the possible redox reactions on the electrochemical reduction of oxygen; the cyclic voltammetric response of all the electrodes in the classical potential ranges between 0.0 and 1.2 V at 30 °C. The typical Pt-peaks obtained on Pt/C and on Pt/TiO_xN_y are around 0.1 and 0.25 V for the hydrogen underpotential deposition (H_{upd}) and around 0.15 and 0.30 V for the oxidation of hydrogen. These peaks are similar to those obtained in our previous works (see for example [58, 59]) and elsewhere (see for example [60]) on the ORR on Pt and the peak current densities of Pt-oxide formation and reduction appear at the same potentials for Pt/C and Pt/TiO_xN_y electrocatalysts.

These peaks indicated that the platinum particles are active when supported by titanium oxy-nitride, agreeing well with the Ref. [61]. The electrochemical surface area is calculated according to the equation [54]:

$$\mathrm{ECSA} = \frac{Q_{\mathrm{H}}}{[\mathrm{Pt}] \cdot 210\,\mu\mathrm{C\,cm^{-2}}} \tag{2}$$

where Q_H is the peak area of hydrogen adsorption–desorption and [Pt] is the platinum loading. ECSA is calculated as 31.2 and 28.0 $m^2\ g^{-1}$ of Pt/TiO_xN_y and Pt/C, respectively. It indicates that the numbers of platinum active sites of Pt/TiO_xN_y and Pt/C are on the same order of magnitude. The ECSA value of Pt/C agrees well with the published data [62]. The BET surface area of Pt/TiO_xN_y is characterized as 73.76 $m^2\ g^{-1}$. The BET surface area is much higher than ECSA since the ECSA is the active site

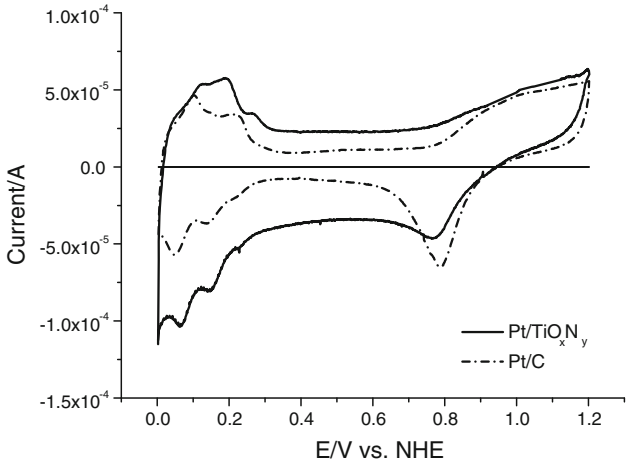

Fig. 5 Cyclic voltammetry of platinum catalyst supported on carbon and titanium oxy-nitride, e.g., Pt/TiO_xN_y and Pt/C

of platinum in the reduction or oxidation process, while the BET surface area is the surface site of physical adsorption. The peaks of the oxide formation and reduction were observed in both curves.

Figure 6a, b shows the slow scan voltage rate curves of the oxygen reduction reaction at 5 mV s^{-1} and 30 °C in oxygen saturated in 0.5 M H_2SO_4 on Pt/TiO_xN_y and Pt/C, respectively. In the activation region, the current density of the ORR on Pt/C and Pt/TiO_xN_y, of course, does not change with the RDE speed. The Tafel plots are derived in the low potential regions (between 0.65 and 0.95 V) of the slow scan voltage rate of curves as shown in Fig. 6. These Tafel plots of the ORR for Pt/C and Pt/TiO_xN_y are shown in Fig. 7. The corresponding Tafel slope, exchange current density, over-potential, and current density at 850 mV are shown in Table 1.

The Tafel slope of the Pt/TiO_xN_y is slightly larger than that of Pt/C which means that the Pt/TiO_xN_y-based electrocatalyst could be less active than the Pt/C-based electrocatalyst for the ORR. Moreover, the current density of Pt/TiO_xN_y in the activation region is lower than that of Pt/C. This may suggest the weaker ability of Pt/TiO_xN_y in the oxygen reduction reaction, although it has more platinum active sites of hydrogen adsorption–desorption. This phenomenon might be caused by the following reasons:

(a) The inhibition of the oxygen diffusion process on the titanium oxy-nitride, which emerged as a smaller limiting current density at low potentials. This might be due to the titanium oxy-nitride conchoidal fracture porous structure which made the platinum particles embedded into titanium oxy-nitride bulk as shown in TEM images. Such a structure might not be favorable to the access of the platinum active sites to oxygen, while carbon is spherical, which is beneficial to oxygen diffusion;

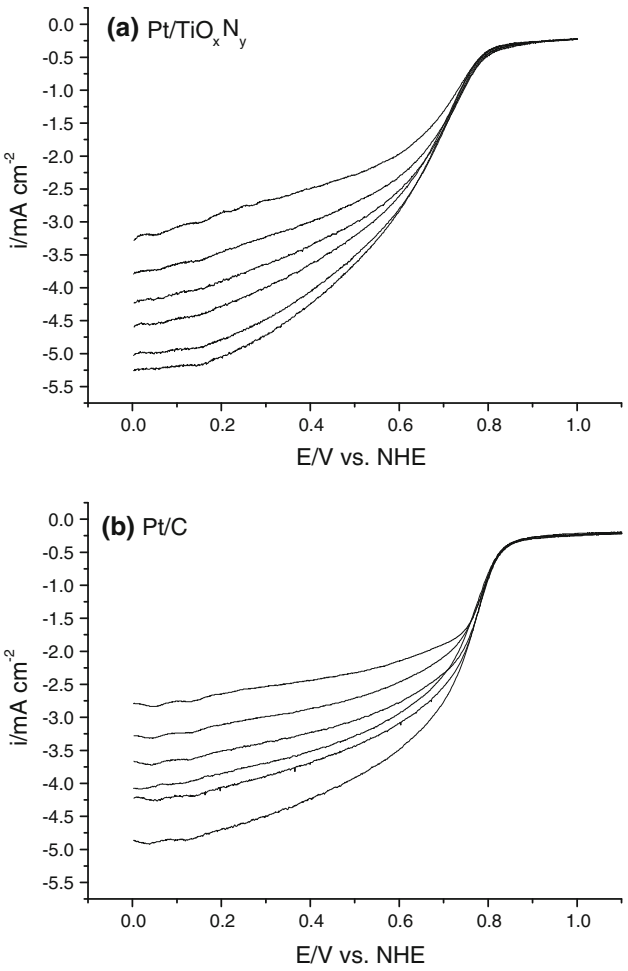

Fig. 6 Slow scan voltage rate curves of the oxygen reduction reaction at 5 mV s^{-1} and 30 °C in oxygen saturated in 0.5 M H_2SO_4 at various rotating speeds of the Rotated Disk Electrode (RDE): **a** Pt/TiO_xN_y and **b** Pt/C

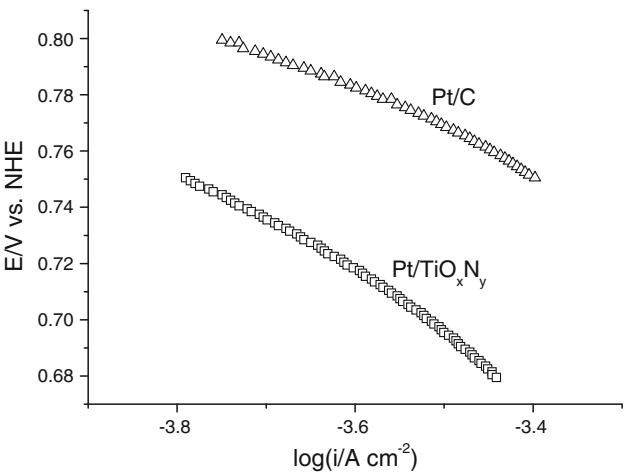

Fig. 7 Tafel plots of the ORR at the low current densities for Pt/TiO_xN_y and Pt/C and from the slow scan voltage rate curves in the anodic sweep direction in the activation region from Fig. 6

Table 1 Electrochemical surface area, exchange current density (i_0), Tafel slope, current density at 850 mV of Pt/TiO_xN_y and Pt/C

	ECSA ($m^2\ g^{-1}$)	i_0 ($mA\ cm^{-2}$)	b ($mV\ dec^{-1}$)	i_{850mV} ($mA\ cm^{-2}$)
Pt/C	28.0	7.89×10^{-3}	123	1.83
Pt/TiO_xN_y	31.2	4.24×10^{-3}	150	1.46

(b) The larger ohmic resistance as a result of the lower electronic conductivity of titanium oxy-nitride than carbon, which was discussed in our previous work [51]. Briefly, the lower performance of Pt/TiO_xN_y for the ORR might suggest a difference in the electrocatalyst support interaction for Pt/C and Pt/TiO_xN_y.

Figure 6 also shows that in the diffusion region, the variation of the ORR current density (i) changes significantly with the RDE rotating speed (ω). These series of ORR polarization curves made at different rotating Disk Electrode speeds can also be used to investigate the difference in kinetics in oxygen reduction reaction and to analyze the interaction between the electrocatalyst and the support. Accordingly, Fig. 8 shows the variation of i^{-1} versus $\omega^{-0.5}$ which are straight lines for different potentials for the ORR on Pt/TiO_xN_y and on Pt/C. These plots can be expressed as the Koutecky–Levich equation [63]:

$$\frac{1}{i} = \frac{1}{i_k} + \frac{1}{i_d} \tag{3}$$

$$i_d = K\omega^{0.5} = 0.62nFD_{O_2}^{2/3}v^{-1/6}C_{O_2}\omega^{0.5} \tag{4}$$

where i is the total ORR current density, i_k is the kinetic current density (in the activation region), and i_d is the diffusion limited current density (in the high ORR reduction potential) where the current is a plateau and its value changes with the RDE rotating speed (ω) in rpm (Fig. 6). This behavior indicates that in these potential regions, the ORR is limited by the oxygen diffusion at the electrode surface and is well described by Eq. 4 where K is the Levich's slope which contains the following parameters: n the number of electron transferred in ORR, F the Faraday constant, C_{O_2} the bulk concentration of oxygen (1.03×10^{-3} mol L^{-1}), D_{O_2} the diffusion coefficient of oxygen in the bulk solution (2.1×10^{-5} $cm^2\ s^{-1}$), and v the kinematic viscosity of the solution (1.07×10^{-2} $cm^2\ s^{-1}$) [64]. From the experimental values of i_d, Eq. 4 is used to determine the value of n. The calculated n values of the Pt/TiO_xN_y and Pt/C are 3.85 and 3.9, respectively. This result indicates that the ORR on the Pt/TiO_xN_y electrocatalyst proceeds via a four-electron transfer process. The kinetic current density i_k is obtained by extrapolation of the Koutecky–Levich plots to $\omega^{-0.5}$ to zero. From Fig. 8, the i_k values of Pt/TiO_xN_y are lower than those of Pt/C. This is an indication that the ORR kinetic rate on Pt/TiO_xN_y might be lower than that of Pt/C, even though the reaction pathway is the same on both electrodes. The low kinetic rate on Pt/TiO_xN_y might be due to the inhibition of the oxygen diffusion on its surface as mentioned above.

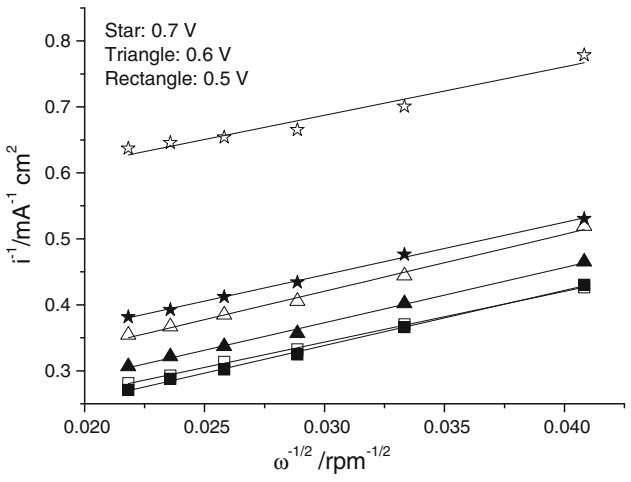

Fig. 8 Koutecky–Levich plots of the ORR reaction in 0.5 M H_2SO_4 at various rotating speeds of the Rotated Disk Electrode (RDE) at various potentials from Fig. 6 of Pt/TiO_xN_y (*hollow*) and Pt/C (*solid*)

Since ORR kinetics proceed via a four-electron transfer process on both electrodes and their electrochemical surface areas are close together, due to its nature, the Pt/TiO_xN_y is more stable than carbon in acid medium. Accordingly, an enhanced durability of Pt/TiO_xN_y could be expected in comparison to that of Pt/C in acid medium similar to PEM fuel cell environment. The electrochemical stability of each of these electrodes was determined by the cyclic voltammetric method. The electrochemical surface area was calculated every hundred cycles. Figure 9 shows the normalized ECSA of Pt/TiO_xN_y and Pt/C variation as a function of the cycling number. As the cycling number increases, the normalized ECSA decreases gradually for both catalysts. Nevertheless, the decrease rate is significantly different for Pt/TiO_xN_y and Pt/C. After 1,000 cycles, ECSA decreases of Pt/TiO_xN_y and Pt/C are 26 and 79 %, respectively. The degradation of Pt/C obtained here is similar to that obtained in the former work [64]. This decrease is mainly due to carbon corrosion. On the other hand, the utilization of TiO_xN_y as Pt catalyst support has clearly enhanced the durability of the catalyst. This result could be ascribed to less corrosion or dissolution of the titanium oxy-nitride than that of carbon. Moreover, it could also be ascribed to the suppressed agglomeration of platinum particles, hence reducing the platinum dissolution.

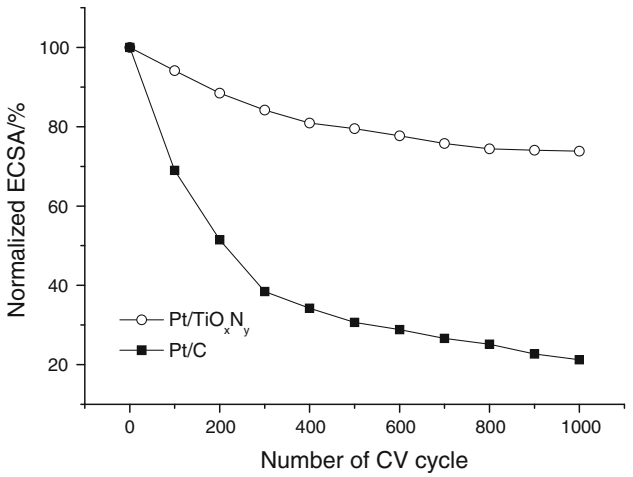

Fig. 9 Normalized electrochemical surface area degradation of Pt/TiO$_x$N$_y$ and Pt/C

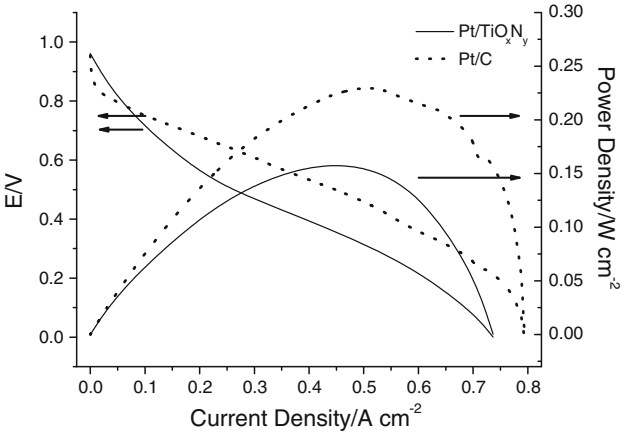

Fig. 10 Potential-current and power density–current density curve performances at 25 °C of a hydrogen/oxygen PEM Fuel Cell using MEA based on Nafion 117 membrane and Pt/TiO$_x$N$_y$ and Pt/C electrode cathode fixed in PEM single-cell hardware

On the other hand, it is found that the as-prepared Pt/TiO$_x$N$_y$ catalyst has a better durability and showed better electrochemical stability after long-term tests. It suggests that the layer structure of the titanium oxy-nitride is acting as an important barrier in preventing aggregation of Pt particles. Such a structure contributes to hindering the aggregation of platinum nanoparticles. Since the interaction between platinum nanoparticles and titanium oxy-nitride does exist, it is more difficult for the platinum nanoparticles to aggregate because the available particles are the surrounding ones in two dimensions, while the particles above or below were separated by titanium oxy-nitride layers. It results in the platinum nanoparticles not being able to grow infinitely. As to Pt/C, the carbon support has a spherical feature, which is suitable for the platinum particles to aggregate. In such an environment, the platinum nanoparticles attached on the surface of the carbon support can touch one another and had more opportunities to aggregate with other Pt particles during the ORR leading to unlimited growth and a wide range of catalyst particle sizes. Moreover, the aggregation of platinum particles might lead to a slight increase in carbon support size that provides less surface area.

The performance of Pt/TiO$_x$N$_y$ in the PEM fuel cell was also investigated. Figure 10 shows the potential-current and power density–current density curves' performances at 25 °C of a hydrogen/oxygen PEM fuel cell using MEA based on Nafion 117 membrane and Pt/TiO$_x$N$_y$ and Pt/C electrode cathode fixed in PEM single cell which provides an active cell surface area of 2.25 cm^2. A 10 % Pt-based electrocatalyst was used at the anode. The potential-current curves of the Pt/C are very similar to those we obtained before under the same conditions [65, 66]. This is an indication that this experimental setup can be used to determine the effect of the support on the performance of the Pt electrocatalyst for PEM fuel cell application. The open circuit voltage of the PEM fuel cell based on Pt/TiO$_x$N$_y$ (0.97 V) electrode is similar to that of the Pt/C electrode (0.99 V). This value of the open circuit voltage of MEA based on Pt/C electrode in this work is the same as that obtained for MEA based on Pt/C electrode in our previous works [65, 66]. The optimum power density of MEA based on Pt/C-based electrode (230 mW cm^{-2}) is higher than those of the Pt/TiO$_x$N$_y$-based electrode (162 mW cm^{-2}). These results support the other results above, which show the low kinetics of the ORR on Pt/TiO$_x$N$_y$ when compared to Pt/C. The slight low performance of the PEM fuel cell based on Pt/TiO$_x$N$_y$ (when compared to that based on Pt/C) might be due to inhibition of oxygen diffusion on the electrocatalyst surface. The very high stability of the Pt/TiO$_x$N$_y$-based electrode (when compared to those based on Pt/C) indicates it might be more suitable for PEM fuel cell application than Pt/C electrocatalyst.

4 Conclusion

Based on the results obtained in this work, it can be concluded that:

(a) A tetragonal structure of titanium oxy-nitride (TiO$_x$N$_y$) as a Pt electrocatalyst support was synthesized by an anhydrous sol–gel. The particle size of the support based on TiO$_x$N$_y$ was 50 nm;
(b) The Pt electrocatalyst with an 8.4 nm particle size was dispersed onto TiO$_x$N$_y$ support by means of the traditional chemical reduction process
(c) Changes in crystallographic parameters of Pt suggest an interaction between the electrocatalyst and the

support. This interaction depends upon the type of the support;

(d) The electrochemical characterization of the Pt/TiO_xN_y and the Pt/C electrodes using cyclic voltammetry, Tafel plots, long-term stability study, and Rotating Disk Electrode shows that Pt/C exhibited better performance for the ORR in acid medium than Pt/TiO_xN_y, but the latter electrode showed better stability than Pt/C in the range of potential of the ORR in PEM fuel cell operating conditions. On both electrodes, the ORR proceeds through a 4-electron process;

(e) Meanwhile, Pt/TiO_xN_y electrode exhibited high electrochemical surface area and improved durability (3 times more stable than Pt/C-based electrode), which makes this electrocatalyst a viable candidate for PEM fuel cell applications;

(f) PEM fuel cell test performed in a single-cell hardware of 2.25 cm^2 showed that MEA based on Pt/TiO_xN_y exhibited good performance, which makes it interesting for further development as a electrocatalyst for the ORR in PEM fuel cell applications;

(g) Future work will focus on optimization of the particle size, geometry, and composition of TiO_xN_y support for Pt in order to get optimized support, which will help to increase the interaction between the support and the electrocatalyst for a better ORR. Evaluation of the corrosion resistant property of Pt/TiO_xN_y-based electrode during more long-term tests of fuel cell will be also done.

Acknowledgments This work has been partially supported by the National Basic Research Program of China (2007CB209705), the National Natural Science Foundation of China (21073120), and the Science and Technology Commission of Shanghai Municipality (09XD1402400, 10520708900).

References

1. Peighambardoust SJ, Rowshanzamir S, Amjadi M (2010) Int J Hydrogen Energy 35:9349–9384
2. Wang Y, Chen KS, Mishler J, Cho SC, Adroher XC (2011) Appl Energy 88:981–1007
3. Bing YH, Liu HS, Zhang L, Ghosh D, Zhang JJ (2010) Chem Soc Rev 39:2184–2202
4. Wu JF, Yuan XZ, Martin JJ, Wang HJ, Zhang JJ, Shen J, Wu SH, Merida W (2008) J Power Sources 184:104–119
5. Yu XW, Ye SY (2007) J Power Sources 172:145–154
6. Centi G, Perathoner S (2010) Catal Today 150:151–162
7. Yousfi-Steiner N, Mocoteguy P, Candusso D, Hissel D (2009) J Power Sources 194:130–145
8. Zhang SS, Yuan XZ, Hin JNC, Wang HJ, Friedrich KA, Schulze M (2009) J Power Sources 194:588–600
9. Lin JF, Adame A, Kannan AM (2010) J Electrochem Soc 157:B846–B851
10. Elezovic NR, Babic BM, Radmilovic VR, Vracar LM, Krstajic NV (2009) Electrochim Acta 54:2404–2409
11. Palchoudhury S, Xu Y, Goodwin J, Bao Y (2011) J Mater Chem 21:3966–3970
12. Chen G, Waraksa CC, Cho H, Macdonald DD, Mallouka TE (2003) J Electrochem Soc 150:E423–E428
13. Ioroi T, Siroma Z, Fujiwara N, Yamazaki SI, Yasuda K (2005) Electrochem Commun 7:183–188
14. Timperman L, Feng YJ, Vogel W, Alonso-Vante N (2010) Electrochim Acta 55:7558–7563
15. Hagihara H, Uchida H, Watanabe M (2006) Electrochim Acta 51:3979–3985
16. Li AZ, Zhao JX, Pierce DT (2010) J Colloid Interface Sci 351:365–373
17. Seger B, Kongkanand A, Vinodgopal K, Kamat PV (2008) J Electroanal Chem 621:198–204
18. Zhu T, Du CY, Liu CT, Yin GP, Shi PF (2011) Appl Surf Sci 257:2371–2376
19. Saha MS, Banis MN, Zhang Y, Li R, Sun X, Cai M, Wagner FT (2009) J Power Sources 192:330–335
20. Shim J, Lee CR, Lee HK, Lee JS, Cairns EJ (2001) J Power Sources 102:172–177
21. Sasaki K, Zhang L, Adzic RR (2008) Phys Chem Chem Phys 10:159–167
22. Suzuki Y, Ishihara A, Mitsushima S, Kamiya N, Ota KI (2007) Electrochem Solid-State Lett 10:B105–B107
23. Zhang Y, Zhang H, Zhai Y, Zhu X, Bi C (2007) J Power Sources 168:323–329
24. Chhina H, Campbell S, Kesler O (2006) J Power Sources 161:893–900
25. Yamaguchi M, Ide-Ektessabi A, Nomura H, Yasui N (2004) Thin Solid Films 447–448:115–118
26. Chhina H, Campbell S, Kesler O (2008) J Power Sources 179:50–59
27. Ganesan R, Lee JS (2005) Angew Chem Int Ed 44:6557–6560
28. Ham DJ, Kim YK, Han SH, Lee JS (2008) Catal Today 132:117–122
29. Jeon MK, Daimon H, Lee KR, Nakahara A, Woo SI (2007) Electrochem Commun 9:2692–2695
30. Antolini E, Gonzalez ER (2009) Solid State Ionics 180:746–763
31. Sato S (1986) Chem Phys Lett 123:126–128
32. Kim SY, Han DH, Kim JN, Lee JJ (2009) J Power Sources 193:570–574
33. Rawal SK, Chawla AK, Chawla V, Jayaganthan R, Chandra R (2010) Appl Surf Sci 256:4129–4135
34. Liu G, Li F, Chen Z, Lu GQ, Cheng H-M (2006) J Solid State Chem 179:331–335
35. Lu C, Zhang J, Li ZQ (2004) J Alloy Compd 381:278–283
36. Yang H, McCormick PG (1993) J Mater Sci 28:5663–5667
37. Song XM, Gopireddy D, Takoudis CG (2008) Thin Solid Films 516:6330–6335
38. Morikawa T, Asahi R, Ohwaki T, Aoki K, Taga Y (2001) Jpn J Appl Phys Part 2 Lett 40:L561–L563
39. Di Valentin C, Finazzi E, Pacchioni G, Selloni A, Livraghi S, Paganini MC, Giamello E (2007) Chem Phys 339:44–56
40. Jagadale TC, Takale SP, Sonawane RS, Joshi HM, Patil SI, Kale BB, Ogale SB (2008) J Phys Chem C 112:14595–14602
41. Kuroda Y, Mori T, Yagi K, Makihata N, Kawahara Y, Nagao M, Kittaka S (2005) Langmuir 21:8026–8034
42. Martinez-Ferrero E, Sakatani Y, Boissiere C, Grosso D, Fuertes A, Fraxedas J, Sanchez C (2007) Adv Funct Mater 17:3348–3354
43. Parida KM, Naik B (2009) J Colloid Interface Sci 333:269–276
44. Chi B, Zhao L, Jin T (2007) J Phys Chem C 111:6189–6193
45. Bellardita M, Addamo M, Di Paola A, Palmisano L, Venezia AM (2009) Phys Chem Chem Phys 11:4084–4093

46. Bacsa R, Kiwi J, Ohno T, Albers P, Nadtochenko V (2005) J Phys Chem B 109:5994–6003
47. Gole JL, Stout JD, Burda C, Lou Y, Chen X (2004) J Phys Chem B 108:1230–1240
48. Li H, Li J, Huo Y (2006) J Phys Chem B 110:1559–1565
49. Sato S, Nakamura R, Abe S (2005) Appl Catal A 284:131–137
50. Kim KH, Lee SH (1996) Thin Solid Films 283:165–170
51. Wang W, Savadogo O, Ma Z-F (2012) Int J Hydrog Energy 37:7405–7417
52. Essalik A, Amouzegar K, Savadogo O (1995) J Appl Electrochem 25:404
53. Ticianelli EA, Derouin CR, Srinivasan S (1988) J Electroanal Chem 251:275
54. Fournier J, Faubert G, Tilquin JY, Cote R, Guay D, Dodelet JP (1997) J Electrochem Soc 144:145–154
55. Gasteiger HA, Panels JE, Yan SG (2004) J Power Sources 127: 162–171
56. Graciani J, Sanz JF, Asaki T, Nakamura K, Rodriguez JA (2007) J Chem Phys 126:244713–244720
57. Avasarala B, Moore R, Haldar P (2010) Electrochim Acta 55:4765–4771
58. Essalik A, Savadogo O, Ajersch F (1995) J Electrochem Soc 142:1368–1376
59. Savadogo O, Essalik A (1996) J Electrochem Soc 143:1812–1814
60. Climent V, Marković NM, Ross PN (2000) J Phys Chem B 104:3116–3120
61. Takenaka S, Matsumori H, Matsune H, Tanabe E, Kishida M (2008) J Electrochem Soc 155:B929–B936
62. Cho YH, Park HS, Cho YH, Jung DS, Park HY, Sung YE (2007) J Power Sources 172:89–93
63. Wang C, Waje M, Wang X, Tang JM, Haddon RC, Yan Y (2003) Nano Lett 4:345–348
64. Chen Z, Waje M, Li W, Yan Y (2007) Angew Chem 119: 4138–4141
65. Tazi B, Savadogo O (2000) Electrochim Acta 45:4329–4339
66. Tian H, Savadogo O (2005) Fuel Cells 5:375–582